Modified self-Kerr-nonlinearity in a four-level N-type atomic system

Jiteng Sheng,[1,*] Xihua Yang,[1,2] Haibin Wu,[3] and Min Xiao[1,†]
[1]*Department of Physics, University of Arkansas, Fayetteville, Arkansas 72701, USA*
[2]*Department of Physics, Shanghai University, Shanghai 200444, China*
[3]*Department of Physics, Duke University, Durham, North Carolina 27708, USA*
(Received 31 August 2011; published 10 November 2011)

The self-Kerr-nonlinearity of a four-level N-type atomic system is studied both experimentally and theoretically. The self-Kerr-nonlinear coefficient n_2 of the probe beam is greatly enhanced near atomic resonance, and can be dramatically modified by changing the switching laser power. With an increasing switching laser power, the slope of the Kerr nonlinear coefficient n_2 around the atomic resonance changes from negative to positive, and the value of n_2 varies from $\sim$–4×10^{-6} to 4×10^{-6} cm^2/W at certain near-resonant probe frequency detunings. Such controllable Kerr nonlinearity can find applications in optoelectronic devices, such as all-optical switching and logic gates.

DOI: 10.1103/PhysRevA.84.053820 PACS number(s): 42.50.Gy, 42.65.−k, 32.80.Qk

I. INTRODUCTION

Great enhancement of the near-atomic resonant nonlinearity with reduced absorption due to quantum interference and atomic coherence is an important feature of electromagnetically induced transparency (EIT) [1]. In the past few years, a number of resonantly enhanced nonlinear phenomena have been observed in EIT-based media, such as frequency conversion [2], four- and six-wave mixing [3–6], EIT-induced beam focusing [7], elimination of optical filamentation [8], and spatial solitons [9]. The greatly enhanced self-Kerr-nonlinearity [10] and cross-Kerr-nonlinearity [11] in three-level EIT systems have been experimentally measured. Although large cross-Kerr-nonlinearity in a four-level N-type atomic system was theoretically predicted [12] and experimentally measured recently [13,14], the self-Kerr-nonlinear properties of such four-level N-type atomic systems have not been explored so far. In this work, we report our experimental investigation of the self-Kerr-nonlinearity in the four-level N-type atomic system. The self-Kerr-nonlinear coefficient n_2 is quantitatively measured in such a four-level N-type atomic system by following the cavity-scanning technique described in Ref. [10]. We have also developed a theoretical model and obtained an analytical solution for the third-order self-Kerr-nonlinearity in the four-level N-type system through the iterative method [10] under the weak-probe approximation. Self-Kerr-nonlinearities in two-, three-, and four-level atomic systems are measured and quantitatively compared in one experimental setup. By simply changing the power of the additional switching laser beam, both the value (as well as the sign) of the self-Kerr-nonlinear coefficient n_2 and its slope near resonance can be altered, which can be very useful in the applications of such greatly enhanced nonlinearity with modified absorption.

The theoretical model is described in Sec. II with the details of the iterative method. In Sec. III, the experimental setup and observations are presented, and the basic principle of measuring the self-Kerr-nonlinear coefficient n_2 from the direct experimental observations is also given. Quantitative comparisons are made between the experimental measurements and the theoretical calculations in Sec. IV. Sec. V serves as the conclusion.

II. THEORETICAL MODEL

We consider a four-level N-type atomic system, as depicted in the inset of Fig. 1. The density-matrix elements under the rotating-wave approximation can be derived by the standard semiclassical method [15]:

$$\dot{\rho}_{11} = \Gamma_{21}\rho_{22} + \Gamma_{31}\rho_{33} + \Gamma_{41}\rho_{44} + \frac{i}{2}(\rho_{31}\Omega_p^* - \rho_{13}\Omega_p), \quad (1a)$$

$$\dot{\rho}_{22} = \Gamma_{42}\rho_{44} + \Gamma_{32}\rho_{33} - \Gamma_{21}\rho_{22} + \frac{i}{2}(\rho_{32}\Omega_c^* - \rho_{23}\Omega_c + \rho_{42}\Omega_s^* - \rho_{24}\Omega_s), \quad (1b)$$

$$\dot{\rho}_{33} = \Gamma_{43}\rho_{44} - \Gamma_{32}\rho_{33} - \Gamma_{31}\rho_{33} + \frac{i}{2}(\rho_{23}\Omega_c - \rho_{32}\Omega_c^* + \rho_{13}\Omega_p - \rho_{31}\Omega_p^*), \quad (1c)$$

$$\dot{\rho}_{44} = -(\Gamma_{43} + \Gamma_{42} + \Gamma_{41})\rho_{44} + \frac{i}{2}(\rho_{24}\Omega_s - \rho_{42}\Omega_s^*), \quad (1d)$$

$$\dot{\rho}_{21} = -\tilde{\gamma}_{21}\rho_{21} - \frac{i}{2}\rho_{23}\Omega_p + \frac{i}{2}\rho_{31}\Omega_c^* + \frac{i}{2}\rho_{41}\Omega_s^*, \quad (1e)$$

$$\dot{\rho}_{31} = -\tilde{\gamma}_{31}\rho_{31} + \frac{i}{2}\rho_{21}\Omega_c + \frac{i}{2}(\rho_{11} - \rho_{33})\Omega_p, \quad (1f)$$

$$\dot{\rho}_{41} = -\tilde{\gamma}_{41}\rho_{41} - \frac{i}{2}\rho_{43}\Omega_p + \frac{i}{2}\rho_{21}\Omega_s, \quad (1g)$$

$$\dot{\rho}_{32} = -\tilde{\gamma}_{32}\rho_{32} + \frac{i}{2}(\rho_{22} - \rho_{33})\Omega_c + \frac{i}{2}\rho_{12}\Omega_p - \frac{i}{2}\rho_{34}\Omega_s, \quad (1h)$$

$$\dot{\rho}_{42} = -\tilde{\gamma}_{42}\rho_{42} - \frac{i}{2}\rho_{43}\Omega_c + \frac{i}{2}(\rho_{22} - \rho_{44})\Omega_s, \quad (1i)$$

$$\dot{\rho}_{43} = -\tilde{\gamma}_{43}\rho_{43} + \frac{i}{2}\rho_{23}\Omega_s - \frac{i}{2}\rho_{42}\Omega_c^* - \frac{i}{2}\rho_{41}\Omega_p^*, \quad (1j)$$

where $\Omega_p = \mu_{13}E_p/\hbar$, $\Omega_c = \mu_{23}E_c/\hbar$, and $\Omega_s = \mu_{24}E_s/\hbar$ are the Rabi frequencies of the probe, coupling, and switching lasers, respectively. We define $\tilde{\gamma}_{21} = \gamma_{21} - i(\Delta_p - \Delta_c)$, $\tilde{\gamma}_{31} =$

*jsheng@uark.edu
†mxiao@uark.edu

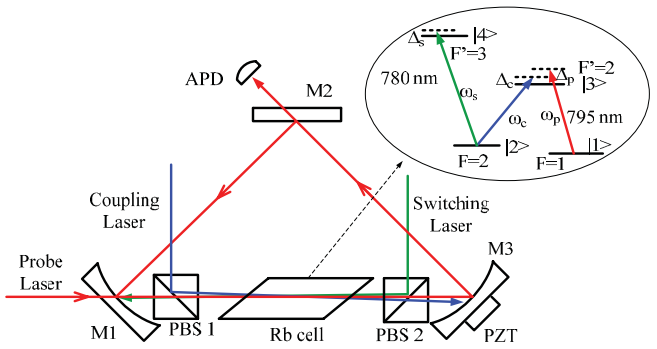

FIG. 1. (Color online) Experimental setup. PBS1 and PBS2: polarization beam splitters; M1-M3: cavity mirrors; APD: avalanche photodiode detector; and PZT: piezoelectric transducer. Inset: four-level atomic system in ^{87}Rb and laser coupling scheme.

$\gamma_{31} - i\Delta_p$, $\tilde{\gamma}_{41} = \gamma_{41} - i(\Delta_p - \Delta_c + \Delta_s)$, $\tilde{\gamma}_{32} = \gamma_{32} - i\Delta_c$, $\tilde{\gamma}_{42} = \gamma_{42} - i\Delta_s$, and $\tilde{\gamma}_{43} = \gamma_{43} - i(\Delta_s - \Delta_c)$ for simplicity. Γ_{nm} are the natural decay rates between level $|n\rangle$ and level $|m\rangle$; and $\gamma_{nm} = \frac{1}{2}(\Gamma_n + \Gamma_m) + \gamma_{nm}^{col}$. Here, $\Delta_p = \omega_p - \omega_{13}$, $\Delta_c = \omega_c - \omega_{23}$, and $\Delta_s = \omega_s - \omega_{24}$ are the probe, coupling, and switching frequency detunings, respectively; and $\gamma_{nm}^{col}$is the collision-induced dephasing rate.

We will use the iterative technique [10] to solve Eq. (1) in the steady state. The density-matrix elements can be expanded as $\rho_{nm} = \rho_{nm}^{(0)} + \rho_{nm}^{(1)} + \rho_{nm}^{(2)} + \rho_{nm}^{(3)} + \cdots$. Here, we make two assumptions: (1) All the populations are in the ground state in the zeroth order, i.e., $\rho_{11}^{(0)} = 1$, $\rho_{22}^{(0)} = \rho_{33}^{(0)} = \rho_{44}^{(0)} = 0$, and (2) the coupling and the switching fields are much stronger than the probe field, that is, $\Omega_p \ll \Omega_s, \Omega_c$. Under the weak-probe approximation, the terms with $\rho_{nm}\Omega_p$ $(n \neq m)$ can be neglected in the equations of the off-diagonal density-matrix elements ρ_{nm} $(n \neq m)$, i.e., Eqs. (1e)–(1i). Solving Eqs. (1e)–(1i) simultaneously, the off-diagonal density-matrix elements, to the first order, can be obtained to be

$$\rho_{21}^{(1)} = -\frac{\tilde{\gamma}_{41}\Omega_p\Omega_c^*}{\tilde{\gamma}_{31}|\Omega_s|^2 + \tilde{\gamma}_{41}|\Omega_c|^2 + 4\tilde{\gamma}_{21}\tilde{\gamma}_{31}\tilde{\gamma}_{41}}, \tag{2a}$$

$$\rho_{31}^{(1)} = \frac{i\Omega_p(|\Omega_s|^2 + 4\tilde{\gamma}_{21}\tilde{\gamma}_{41})}{2(\tilde{\gamma}_{31}|\Omega_s|^2 + \tilde{\gamma}_{41}|\Omega_c|^2 + 4\tilde{\gamma}_{21}\tilde{\gamma}_{31}\tilde{\gamma}_{41})}, \tag{2b}$$

$$\rho_{41}^{(1)} = -\frac{i\Omega_p\Omega_s\Omega_c^*}{2(\tilde{\gamma}_{31}|\Omega_s|^2 + \tilde{\gamma}_{41}|\Omega_c|^2 + 4\tilde{\gamma}_{21}\tilde{\gamma}_{31}\tilde{\gamma}_{41})}, \tag{2c}$$

$$\rho_{32}^{(1)} = \rho_{42}^{(1)} = \rho_{43}^{(1)} = 0. \tag{2d}$$

Since in a closed atomic system the total population is conserved, i.e., $\rho_{11} + \rho_{22} + \rho_{33} + \rho_{44} = 1$, it is straightforward to find the second-order diagonal density-matrix elements satisfying the relationship

$$\rho_{11}^{(2)} + \rho_{22}^{(2)} + \rho_{33}^{(2)} + \rho_{44}^{(2)} = 0. \tag{3}$$

Substituting Eqs. (2a)–(2d) into the equations of the diagonal density-matrix elements ρ_{nn} [Eqs. (1a)–(1d)], and solving them simultaneously with Eq. (3), the diagonal density-matrix elements can be obtained, up to the second order, to be

$$\rho_{11}^{(2)} = -\frac{(\Gamma_{21} + \Gamma_{32})|\Omega_p|^2}{4\Gamma_{21}(\Gamma_{31} + \Gamma_{32})}\left(\frac{1}{F} + \frac{1}{F^*}\right), \tag{4a}$$

$$\rho_{22}^{(2)} = \frac{\Gamma_{32}|\Omega_p|^2}{4\Gamma_{21}(\Gamma_{31} + \Gamma_{32})}\left(\frac{1}{F} + \frac{1}{F^*}\right), \tag{4b}$$

$$\rho_{33}^{(2)} = \frac{|\Omega_p|^2}{4(\Gamma_{31} + \Gamma_{32})}\left(\frac{1}{F} + \frac{1}{F^*}\right), \tag{4c}$$

$$\rho_{44}^{(2)} = 0, \tag{4d}$$

where

$$F = \tilde{\gamma}_{31} + \frac{|\Omega_c|^2/4}{\tilde{\gamma}_{21} + \frac{|\Omega_s|^2/4}{\tilde{\gamma}_{41}}}.$$

Substituting Eqs. (4a)–(4d) into the equations of the off-diagonal density-matrix elements [Eqs. (1e)–(1i)], and solving them again, can yield the following result:

$$\rho_{31}^{(3)} = -\frac{i\Omega_p|\Omega_p|^2}{8F}\frac{2\Gamma_{21} + \Gamma_{32}}{\Gamma_{21}(\Gamma_{31} + \Gamma_{32})}\left(\frac{1}{F} + \frac{1}{F^*}\right). \tag{5}$$

From the definitions $\chi = \frac{2N\mu_{13}}{\varepsilon_0 E_p}\rho_{31}$, $\chi = \chi^{(1)} + 3|E_p|^2\chi^{(3)}$, and $n = n_0 + n_2 I$ [16], the third-order susceptibility is obtained as

$$\chi^{(3)} = -\frac{iN|\mu_{13}|^4}{12\varepsilon_0\hbar^3}\frac{2\Gamma_{21} + \Gamma_{32}}{\Gamma_{21}(\Gamma_{31} + \Gamma_{32})}\frac{1}{F}\left(\frac{1}{F} + \frac{1}{F^*}\right), \tag{6}$$

and the self-Kerr-nonlinear coefficient n_2 is given by $\frac{3\mathrm{Re}\chi^{(3)}}{c\varepsilon_0}$. Here c is the speed of light in vacuum and ε_0 is the vacuum permittivity.

Considering the Doppler effect in an atomic vapor cell, we replace Δ_p, Δ_c, and Δ_s by $\Delta_p + k_p v$, $\Delta_c + k_c v$, and $\Delta_s - k_s v$; then the third-order susceptibility is given by

$$\chi^{(3)}(v) = \int_{-\infty}^{\infty} -\frac{iN(v)|\mu_{13}|^4}{12\varepsilon_0\hbar^3}\frac{2\Gamma_{21} + \Gamma_{32}}{\Gamma_{21}(\Gamma_{31} + \Gamma_{32})}\frac{1}{F(v)} \times\left[\frac{1}{F(v)} + \frac{1}{F(v)^*}\right]dv. \tag{7}$$

Here we only consider the case where both the coupling and the switching lasers are on resonance ($\Delta_c = \Delta_s = 0$); therefore, F is reduced to

$$F(v) = \gamma_{31} - i(\Delta_p + kv) + \frac{|\Omega_c|^2/4}{\gamma_{21} - i[(\Delta_p + kv) - (\Delta_c + kv)] + \frac{|\Omega_s|^2/4}{\gamma_{41} - i[(\Delta_p + kv) - (\Delta_c + kv) + (\Delta_s - kv)]}},$$

$$= \gamma_{31} - i(\Delta_p + kv) + \frac{|\Omega_c|^2/4}{\gamma_{21} - i\Delta_p + \frac{|\Omega_s|^2/4}{\gamma_{41} - i(\Delta_p - kv)}}, \tag{8}$$

where $k_p \approx k_c \approx k_s \equiv k$ is the wave number of the electromagnetic field. The atomic speeds obey a Maxwell-Boltzmann distribution, which yields a Gaussian distribution for the velocity $N(v) = \frac{N_0}{u\sqrt{\pi}} e^{-v^2/u^2}$. Here $u/\sqrt{2}$ is the root mean square atomic velocity, and $\Delta\omega_D = 2\sqrt{\ln 2}ku$ is the full width at half maximum (FWHM) of the Doppler width of the thermal atomic distribution.

III. EXPERIMENTAL MEASUREMENTS

The experimental setup is shown in Fig. 1, which is similar to the one used in Ref. [17]. The probe, coupling, and switching lasers are single-mode lasers (Toptica DL 100) with current and temperature stabilized. A three-mirror optical ring cavity consists of an input mirror M1 and an output mirror M2 with 3% and 1.4% transmissivities, respectively, and a third mirror M3 with reflectivity larger than 99.5%, mounted on a piezoelectric transducer (PZT) for cavity frequency scanning and locking. M1 and M3 are curved mirrors with a 10-cm radius of curvature. The optical path length of the ring cavity is ~37 cm. The rubidium vapor cell, without buffer gas, is 5 cm long with Brewster windows, and is wrapped in a μ-metal sheet for magnetic shielding and in heat tape for controlling the temperature. Four energy levels in the D line of ^{87}Rb atom are used for the N-type four-level system, as shown in the inset of Fig. 1. The coupling (ω_c) and switching (ω_s) laser beams are injected separately through two polarization beam splitters (PBS 1 and PBS 2) and counterpropagate through the vapor cell. The probe (ω_p) beam is injected into the cavity via the input mirror M1 and circulates in the cavity as the cavity field. The output of the cavity is detected by an avalanche photodiode detector (APD). The coupling beam copropagates with the cavity field, and has a small misalignment with the cavity axis to avoid its circulation in the cavity. The switching beam is carefully aligned to obtain good overlaps with other beams in the vapor cell by monitoring the absorption. The radii of the coupling, switching, and probe laser beams are estimated to be 400, 400, and 100 μm at the center of the atomic cell, respectively. The empty cavity finesse is ~100. When the atomic cell, two PBSs, and a diaphragm (as a mode cleaner) are inserted into the cavity, the cavity finesse degrades down to ~40. An additional frequency-stabilized diode laser is used to lock the optical ring cavity (not shown in Fig. 1). Both the coupling and switching lasers are locked on the saturated absorption spectrum with $\Delta_c = \Delta_s = 0$ using another atomic cell. The probe laser is locked on a Fabry-Perot cavity, and by tuning the applied voltage on the PZT of the Fabry-Perot cavity, the probe laser frequency can be easily detuned within a range of several hundred megahertz. With another Fabry-Perot cavity and the saturated absorption spectrum, the exact value of the probe frequency detuning can be determined.

By scanning the ring cavity, the cavity transmission spectrum shows a typical symmetric Lorentzian shape when the probe beam is tuned far from the atomic resonances (linear intracavity medium). When the probe (cavity) field is tuned to near the atomic resonance, the cavity transmission profile becomes asymmetric due to the self-Kerr-nonlinear coefficient n_2 and the degree of such asymmetry is a direct measure of the Kerr nonlinearity [10]. Figure 2 shows the cavity transmissions

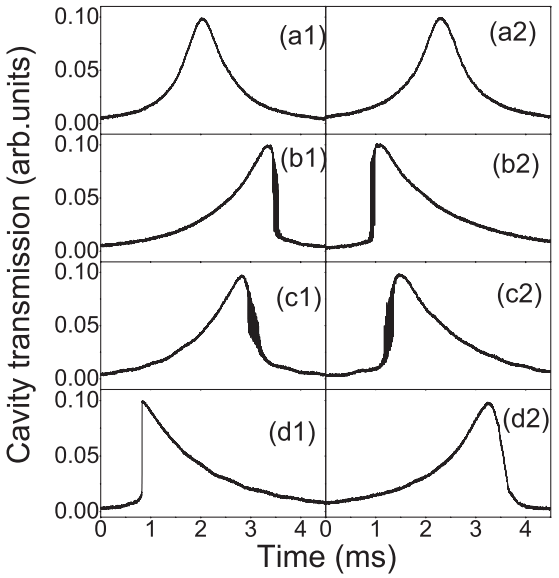

FIG. 2. Cavity transmissions with the scan of the cavity length scanning. (a1) $\Delta_p/2\pi = 14$ MHz, $P_c = P_s = 0$; (b1) $\Delta_p/2\pi = 14$ MHz, $P_c = 13.3$ mW, $P_s = 0$; (c1) $\Delta_p/2\pi = 14$ MHz, $P_c = 13.3$ mW, $P_s = 0.4$ mW; (d1) $\Delta_p/2\pi = 14$ MHz, $P_c = 13.3$ mW, $P_s = 2.7$ mW; (a2) $\Delta_p/2\pi = -14$ MHz, $P_c = P_s = 0$; (b2) $\Delta_p/2\pi = -4$ MHz, $P_c = 13.3$ mW, $P_s = 0$; (c2) $\Delta_p/2\pi = -14$ MHz, $P_c = 13.3$ mW, $P_s = 0.4$ mW; (d2) $\Delta_p/2\pi = -14$ MHz, $P_c = 13.3$ mW, $P_s = 2.7$ mW. Other experimental parameters are $T = 66$ °C and $\Delta_c = \Delta_s = 0$.

under several different experimental conditions. Figures 2(a1) and 2(a2) are for the two-level cases with the coupling and switching beams turned off. Figures 2(b1) and 2(b2) are for the three-level cases with only the switching beam turned off. Figures 2(c1) and 2(c2) are for the four-level cases with a relatively weak switching laser beam and Figs. 2(d1) and 2(d2) are for the four-level cases with a relatively strong switching laser beam. The left and right columns of Fig. 2 correspond to the situations when $\Delta_p/2\pi = 14$ and -14 MHz, respectively. When the cavity length is scanned from shorter to longer, the left part of the peak becomes more gradual, while the right part of the peak becomes steeper if n_2 is negative, as shown in Fig. 2(b1). The opposite is true when the value of n_2 is positive. The self-Kerr-nonlinear coefficient n_2 can be directly determined by the degree of asymmetry ($\Delta = t_1 + t_2 - 2t_p$) of the peak as $n_2 = \frac{\lambda\Delta}{\tau I_p l}$ [10]. Here, λ is the wavelength, τ is the time period between two transmission peaks, I_p is the peak intensity, l is the length of the rubidium cell, and t_1, t_2 are the times on two sides of the peak at which the output intensity is half of the peak intensity, respectively. Therefore, from Fig. 2, it is easy to see that when $\Delta_p/2\pi = 14$ MHz, n_2 is very small in the two-level case due to its almost symmetric transmission peak; n_2 has a negative value when the coupling beam is applied [Fig. 2(b1)]; the absolute value of n_2 decreases (i.e., a smaller negative value) when a weak switching beam is applied [Fig. 2(c1)] since the degree of the asymmetry reduces; and n_2 changes sign when a strong switching beam is applied [Fig. 2(d1)]. Similar discussions can be used for Figs. 2(a2)–2(d2) with the sign of n_2 switched. During the experimental measurements under

different conditions, the intracavity peak power has been kept at ~50 μW ($\Omega_p \approx 2\pi \times 10$ MHz) by adjusting the input probe laser power to compensate for the changes in absorption under different laser beam configurations and powers.

IV. COMPARISONS AND DISCUSSION

Figure 3 shows both the experimentally measured and theoretically calculated self-Kerr-nonlinear coefficients (n_2) versus the probe frequency detuning for different atomic energy level configurations. The theoretical simulations are carried out according to Eq. (7) with the Doppler effect included. The key parameters in the experiments are, for each panel, (a1) $P_c = P_s = 0$; (b1) $P_c = 13.3$ mW ($\Omega_c \approx 2\pi \times 120$ MHz), $P_s = 0$; (c1) $P_c = 13.3$ mW, $P_s = 0.4$ mW ($\Omega_s \approx 2\pi \times 35$ MHz); (d1) $P_c = 13.3$ mW, $P_s = 2.7$ mW ($\Omega_s \approx 2\pi \times 91$ MHz). The frequency detunings for the coupling and switching beams are kept as zero. In the calculations, the parameters used are $\gamma_{21} = 2\pi \times 1$ MHz, $\gamma_{31} = \gamma_{41} = 2\pi \times 130$ MHz, $\Delta\omega_D = 2\pi \times 540$ MHz with (a2) $\Omega_c = \Omega_s = 0$; (b2) $\Omega_c = 2\pi \times 100$ MHz, $\Omega_s = 0$; (c2) $\Omega_c = 2\pi \times 100$ MHz, $\Omega_s = 2\pi \times 35$ MHz; and (d2) $\Omega_c = 2\pi \times 100$ MHz, $\Omega_s = 2\pi \times 120$ MHz. The large γ_{31} and γ_{41} values taken for the calculation may come from several factors. Under current experimental conditions, the main contributions are from the power broadening and collisional dephasing. The

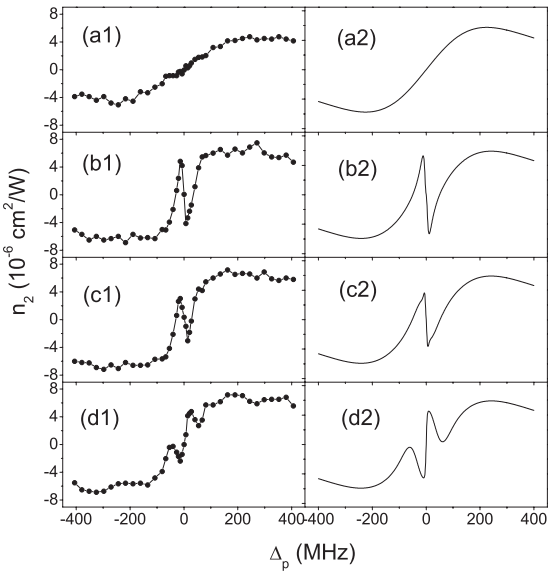

FIG. 3. Self-Kerr-nonlinear coefficients n_2 versus probe frequency detuning. The left column presents the experimentally measured results and the right column gives the corresponding theoretically calculated curves. (a1) and (a2) are for the two-level cases; (b1) and (b2) are for the three-level cases; (c1) and (c2) are for the four-level cases at a relatively small switching laser power; and (d1) and (d2) are for the four-level cases at a relatively strong switching laser power. The experimental parameters are $P_s = 0$, 0.4 mW, and 2.7 mW in (b1), (c1), and (d1), respectively. Other experimental parameters are the same as in Fig. 2. The theoretical parameters are $\gamma_{21} = 2\pi \times 1$ MHz, $\gamma_{31} = \gamma_{41} = 2\pi \times 130$ MHz, $\Delta\omega_D = 2\pi \times 540$ MHz with (a2) $\Omega_c = \Omega_s = 0$; (b2) $\Omega_c = 2\pi \times 100$ MHz, $\Omega_s = 0$; (c2) $\Omega_c = 2\pi \times 100$ MHz, $\Omega_s = 2\pi \times 35$ MHz; and (d2) $\Omega_c = 2\pi \times 100$ MHz, $\Omega_s = 2\pi \times 120$ MHz.

maximum values of the self-Kerr-nonlinear coefficient n_2 for the four-level system [Fig. 3(c1)] can reach ~4×10^{-6} cm^2/W with dramatic change near the atomic resonance similar to the case of the three-level system [Fig. 3(b1)] [10]. As one can see from Figs. 3(c1) and 3(d1), with an increase in the switching laser power, the slope of n_2 near the atomic resonance changes from negative to positive. Specifically, under strong switching laser power, as shown in Figs. 3(d1) and 3(d2), the line shape of n_2 can be understood as a superposition of three curves of the nonlinear coefficients from three atomic resonances [18]. The dependence of the self-Kerr-nonlinear coefficients n_2 versus the switching laser power P_s at $\Delta_p/2\pi = 14$ MHz is depicted in Fig. 4. The dots with error bars (statistical errors) are the experimental data, and the solid line is a theoretical fitting using Eq. (7). From Fig. 4, it is clear that the Kerr nonlinear coefficient n_2 can be dramatically modified at certain near-resonant probe frequency detunings, even switching the sign, just by changing the switching laser power. Such change of sign for nonlinear coefficient (or nonlinear dispersion slope) by controlling the switching beam power can be used in compensating the sharp linear dispersion change [19] to achieve the "white-light cavity" condition for the intracavity EIT medium, as done in the three-level EIT medium [20], with an additional control parameter.

Equation (7) is actually a general solution which includes the cases for two-level, three-level, and four-level systems. There are a large number of parameters that can be adjusted. We can also calculate the theoretical curve for the self-Kerr-nonlinearity as a function of the frequency detuning of the switching beam (Δ_s). However, the experimental measurements for such detuning case become complicated due to the closely lying hyperfine levels of the rubidium D_2 line, which are all within the Doppler-broadened spectrum. We would also like to point out that the self-Kerr-nonlinearity studied here is different from the cross-Kerr-nonlinearity studied in the earlier works [13,14]. The cross-Kerr-nonlinearity is proportional to $n_2' I_s$, which corresponds to the term of $|\Omega_s|^2$ in the first-order solutions in Eq. (2b), while the self-Kerr-nonlinearity we studied here is proportional to $n_2 I_p$, which is the feature of the third-order solutions for the probe beam. These two different kinds of Kerr nonlinearities have very different applications [9,12].

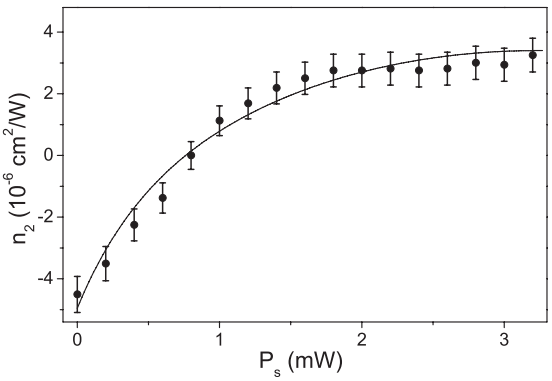

FIG. 4. Experimentally measured (dots with error bars) and theoretically calculated (solid line) self-Kerr-nonlinear coefficients (n_2) as a function of P_s at $\Delta_p/2\pi = 14$ MHz. Other parameters are the same as in Fig. 3.

V. CONCLUSION

We have directly measured the self-Kerr-nonlinear coefficient n_2 in a four-level N-type atomic system by using the cavity scanning technique, which has the advantage of taking out the contributions from the linear absorptions of the laser beams. A set of coupled equations of density-matrix elements and the iteration technique were used to calculate the third-order susceptibility $\chi^{(3)}$ for the multilevel atomic systems with Doppler effect included. Comparisons were made between the experimentally measured and theoretically calculated self-Kerr-nonlinear indices for the two-, three-, and four-level systems. Although the four-level N-type atomic system has the same magnitude of the self-Kerr-nonlinear coefficient as the three-level system, the power of the additional switching beam can control the magnitude, as well as the sign (slope), of the Kerr nonlinearity near the atomic resonance with coupling and switching beams tuned to resonance. Such greatly enhanced and controllable self-Kerr-nonlinearity can be used to construct efficient all-optical switching and logic gates for classical and quantum communication applications.

ACKNOWLEDGMENT

We acknowledge the funding support of the National Science Foundation.

[1] S. E. Harris, Phys. Today **50**, 36 (1997).
[2] M. Jain, H. Xia, G. Y. Yin, A. J. Merriam, and S. E. Harris, Phys. Rev. Lett. **77**, 4326 (1996).
[3] P. R. Hemmer *et al*., Opt. Lett. **20**, 982 (1995).
[4] Y. Li and M. Xiao, Opt. Lett. **21**, 1064 (1996); B. Lü, W. H. Burkett, and M. Xiao, *ibid*. **23**, 804 (1998).
[5] H. Kang, G. Hernandez, and Y. Zhu, Phys. Rev. Lett. **93**, 073601 (2004).
[6] Y. Zhang, U. Khadka, B. Anderson, and M. Xiao, Phys. Rev. Lett. **102**, 013601 (2009).
[7] R. R. Moseley, S. Shepherd, D. J. Fulton, B. D. Sinclair, and M. H. Dunn, Phys. Rev. Lett. **74**, 670 (1995).
[8] M. Jain, A. J. Merriam, A. J. Kasapi, G. Y. Yin, and S. E. Harris, Phys. Rev. Lett. **75**, 4385 (1995).
[9] Y. Zhang, Z. Wang, Z. Nie, C.Li, H. Chen, K. Lu, and M. Xiao, Phys. Rev. Lett. **106**, 093904 (2011).
[10] H. Wang, D. Goorskey, and M. Xiao, Phys. Rev. Lett. **87**, 073601 (2001); J. Mod. Opt. **49**, 335 (2002).
[11] H. Chang, Y. Du, J. Yao, C. Xie, and H. Wang, Europhys. Lett. **65**. 485 (2004).
[12] H. Schmidt and A. Imamoglu, Opt. Lett. **21**, 1936 (1996).
[13] H. Kang and Y. Zhu, Phys. Rev. Lett. **91**, 093601 (2003).
[14] H.-Y. Lo, Y.-C. Chen, P.-C. Su, H.-C. Chen, J.-X. Chen, Y.-C. Chen, I. A. Yu, and Y.-F. Chen, Phys. Rev. A **83**, 041804(R) (2011).
[15] M. O. Scully and M. S. Zubairy, *Quantum Optics* (Cambridge University Press, 1997).
[16] R. W. Boyd, *Nonlinear Optics* (Academic, New York, 1992).
[17] J. Sheng, X. Yang, U. Khadka, and M. Xiao, Opt. Express **19**, 17059 (2011).
[18] T. Y. Abi-Salloum, B. Henry, J. P. Davis, and F. A. Narducci, Phys. Rev. A **82**, 013834 (2010).
[19] M. Xiao, Y. Q. Li, S. Z. Jin, and J. Gea-Banacloche, Phys. Rev. Lett. **74**, 666 (1995).
[20] H. Wu and M. Xiao, Phys. Rev. A, **77**, 031801(R) (2008).